Chinese Chemical Letters 36 (2025) 110396

Contents lists available at ScienceDirect

Chinese Chemical Letters

journal homepage: www.elsevier.com/locate/cclet

Interface engineering of Pt/CeO_2-{100} catalysts for enhancing catalytic activity in auto-exhaust carbon particles oxidation

Peng Zhang[a,1], Yitao Yang[a,1], Tian Qin[b,1], Xueqiu Wu[a], Yuechang Wei[a,*], Jing Xiong[a], Xi Liu[b,c], Yu Wang[d,*], Zhen Zhao[a], Jinqing Jiao[e,*], Liwei Chen[b]

[a] State Key Laboratory of Heavy Oil Processing, Key Laboratory of Optical Detection Technology for Oil and Gas, College of Science, China University of Petroleum, Beijing 102249, China
[b] School of Chemistry and Chemical, In-situ Center for Physical Sciences, Frontiers Science Center for Transformative Molecules, Shanghai Jiao Tong University, Shanghai 200240, China
[c] School of Chemistry and Chemical Engineering, Ningxia University, Yinchuan 750021, China
[d] School of Environmental Science and Engineering, Yancheng Institute of Technology, Yancheng 224051, China
[e] State Key Laboratory of Chemical Safety, SINOPEC Research Institute of Safety Engineering Co., Ltd., Qingdao 266071, China

ARTICLE INFO

Article history:
Received 31 May 2024
Revised 28 August 2024
Accepted 30 August 2024
Available online 31 August 2024

Keywords:
Pt NPs
Defective ceria
Nanocube
Catalytic oxidation
Soot particles

ABSTRACT

Herein, we fabricate an embedding structure at the interface between Pt nanoparticles (NPs) and CeO_2-{100} nanocubes with surface defect sites (CeO_2-SDS) through quenching and gas bubbling-assisted membrane reduction methods. The *in-situ* substitution of Pt NPs for atomic-layer Ce lattice significantly increases the amount of reactive oxygen species from 133.68 μmol/g to 199.44 μmol/g. As a result, the distinctive geometric structure of Pt/CeO_2-SDS catalyst substantially improves the catalytic activity and stability for soot oxidation compared with the catalyst with no quenching process, *i.e.*, its T_{50} and TOF values are 332 °C and 2.915 h^{-1}, respectively. Combined with the results of experimental investigations and density functional theory calculations, it is unveiled that the unique embedding structure of Pt/CeO_2-SDS catalyst can facilitate significantly electron transfer from Pt to the CeO_2-{100} support, and induce the formation of interfacial [Ce-O_x-Pt_2] bond chains, which plays a crucial role in enhancing the key step of soot oxidation through the dual activation of surface lattice oxygen and molecular O_2. Such a fundamental revelation of the interfacial electronic transmission and corresponding modification strategy contributes a novel opportunity to develop high-efficient and stable noble metal catalysts at the atomic level.

Auto-exhaust carbon (soot) particles with adsorbed toxic substances have imperiled human health and environmental sustainability [1,2]. The after-treatment technology is still an indispensable section for soot abatement, where the high-efficient oxidation of soot particles by catalysts coated on diesel/gasoline particulate filters (G/DPFs) is always a major focus in this field [3]. The catalytic oxidation of soot particles is a typical heterogeneous oxidation, which takes place at the triple-phase contact among solid carbon particles, gaseous reactants (O_2 and NO) and solid catalysts [4–7]. To achieve top oxidation performance, the majority of research focuses on the surface modulation of catalysts to increase the amount of reactive oxygen species (ROSs), which play a dominant role in soot oxidation. Oxide-supported noble metal (Pt, Pd, Ag, *etc.*) catalysts have received extensive attention in this field [8–11], where the adjustable metal-support interaction (MSI) is generally accepted as one of the key factors for enhancing catalytic activity.

Platinum (Pt) supported on CeO_2, known for its exceptional catalytic performance in various reactions, is a highly attractive catalyst system, particularly in the field of environmental remediation [12]. It was reported their MSI can be modulated by the following factors, including the morphology or exposed crystal facet [13-15], the density of defects [16,17], and temperature and atmosphere of heat treatment [18,19]. These factors contribute to both the geometric and electronic effects of the catalysts. Among them, the embedding structure where the Pt atoms enter the CeO_2 surface has attracted much attention. Since the binding energy of Pt atoms in metals is lower than their binding energy with CeO_2, single-atom Pt can be easily embedded or adsorbed onto CeO_2 surface

* Corresponding authors.
E-mail addresses: weiyc@cup.edu.cn (Y. Wei), wy252@126.com (Y. Wang), jiaojq.qday@sinopec.com (J. Jiao).
[1] These authors contributed equally to this work.

https://doi.org/10.1016/j.cclet.2024.110396
1001-8417/

[20]. However, the intrinsic activity of atomic dispersed Pt atoms in heterogeneous oxidation is often lower than that of Pt NPs [21]. Recently, it was reported that the exposed crystal facets impose great influence on the embedding structure of Pt particles or clusters [22,23]. Through the equal volume impregnation method, Pt clusters can easily form an embedded structure with the CeO_2-{110} surface, but not with the CeO_2-{100} surface [23]. Thereby, the Pt/CeO_2-{100} catalyst exhibits inferior stability during long-term reaction. The high mobility of Pt NPs also poses a huge challenge to establishing stable Pt NPs on CeO_2-{100} support.

Herein, we fabricate an embedding structure at the interface between Pt nanoparticles (NPs) and CeO_2-{100} nanocubes with surface defect sites (CeO_2-SDS) through quenching and gas bubbling-assisted membrane reduction (GBMR) methods, where Pt NPs (~4.21 nm) are embedded within 5–6 atomic layers of the CeO_2-{100} surface lattice. The unique embedding structure of Pt/CeO_2-SDS catalyst presents superior catalytic activity and stability for soot oxidation compared with the catalyst with no quenching process. Through a systemic combination of experimental results and DFT calculations, the inner reasons for enhancing interfacial electronic transmission and reaction mechanisms were elaborately revealed. The modulated strategy for anchoring Pt NPs on the CeO_2 {100} facet provides a promising opportunity to develop high-efficient and stable Pt-based catalysts for thermal heterogeneous catalysis.

In Fig. S1 (Supporting information), XRD patterns confirm the crystal structure of cubic CeO_2 (JCPDS No. 34-0394, Fm-3m) [9]. The grain size calculated through Scherrer equation is between 28 nm and 32 nm, indicating that the influence of quenching on the bulk phase is negligible. The characteristic diffraction peak of Pt NPs (39.8°) was not detected, which indicates the high dispersion and small size of Pt NPs. The actual loading amount of Pt NPs over Pt/CeO_2 and Pt/CeO_2-SDS catalysts is close to their theoretical value, which are 1.2 wt% and 1.3 wt%, respectively (Table S1 in Supporting information). The specific surface area (S_{BET}), pore volume (V_p), and pore diameter (D_p) of CeO_2-based catalysts are maintained at 23–26 m^2/g, 0.17–0.18 cm^3/g, and 13.6–15.3 nm, respectively (Fig. S2 and Table S1 in Supporting information). As shown in Fig. S1, the strong Raman peak centered at 454 cm^{-1} is designated to the first-order F_{2g} symmetry of CeO_2 [24]. Other peaks at 254, 585, and 1170 cm^{-1} are ascribed to the second-order transverse acoustic mode, defect-induced mode, and second-order longitudinal optical mode of the fcc CeO_2, respectively [25]. The peak intensity ratio at 585 cm^{-1} to at 454 cm^{-1} (I_{585}/I_{454}) can be used to calculate the concentration of oxygen vacancies (O_{Vs}). As summarized in Table S1, the I_{585}/I_{454} value increases from 0.05 to 0.10 after quenching, which can promote the adsorption and activation of molecular O_2. After supporting Pt NPs, a vibrational peak belonging to the Pt-O bond appears at 657 cm^{-1} [26]. The I_{585}/I_{454} value of Pt/CeO_2-SDS (0.21) catalyst is higher than that of Pt/CeO_2 catalyst (0.12), indicating the embedding structure further boosts the formation of O_{Vs}.

Aberration-corrected STEM images (Figs. 1a and b) demonstrate that the CeO_2 catalyst presents a cubic morphology with exposed {100} facet [13]. The smooth surface implies perfect crystallization. After quenching, abundant surface steps directly confirm the increase in surface defects (Figs. 1c and d), supporting the above Raman results. As can be seen from Figs. 1e, f, i and j, and Fig. S3 (Supporting information), Pt NPs are evenly distributed on both supports, whose mean particle sizes (d_{mean}) over Pt/CeO_2 and Pt/CeO_2-SDS catalysts are 5.02 and 4.21 nm, respectively (Fig. S4 in Supporting information). Additionally, it is notable that the micromorphology of Pt NPs on Pt/CeO_2 catalyst is semi-ellipsoidal, and an easily distinguishable interface between Pt NPs and CeO_2 support is observed (Fig. 1g). With the aid of the corresponding bright field STEM image (Fig. S3c), surface and interior lattice fringes are identified as Pt (111) and CeO_2 (220) facets, respectively. In contrast, benefiting from the quenching-induced surface steps, both flathead and semi-ellipsoidal Pt NPs coexist on the Pt/CeO_2-SDS catalyst and form an embedding structure (Fig. 1k). The bottom few layers of the Pt NPs are trapped in CeO_2-SDS support, which can enhance the MSI, thus boosting the catalytic performance. Then, the electron energy loss spectroscopy (EELS) of Ce $M_{4,5}$-edge and O K-edge were further collected, where the spectra 1–3 in Figs. 1h and l correspond to the regions 1–3 in Figs. 1g and k, respectively. Two peaks of 891.5 and 910.2 eV were detected in the interior (region 1) of both Pt/CeO_2 and Pt/CeO_2-SDS catalysts. Combined with the corresponding O K-edge EELS spectra (Fig. S3), they are identified as the characteristic peaks of CeO_2 (Ce^{4+} ions) [27]. Moreover, the predominant form of Ce elements at the interface of CeO_2 support and Pt NPs (region 2) is still Ce^{4+} ion. At region 3 of the Pt/CeO_2 catalyst, the signal of Ce $M_{4,5}$-edge was not detected on the surface of Pt NPs, which is in good agreement with the easily distinguishable interfacial structure described above. For the Pt/CeO_2-SDS catalyst, the increased intensity ratio of M_5/M_4 and the energy shift to the low energy side indicate the formation of the low-valent Ce^{3+} ions [27]. The transformation can be summarized as follows: Ce^{4+}-O^{2-}-Ce^{4+}-O^{2-}-$Ce^{4+} \rightarrow Ce^{3+}$-$O_V$-$Pt^{2+}$-$O_V$-$Ce^{3+}$. It further confirms the embedding structure that the bottom layers of the Pt NPs are anchored by the surface defects of the CeO_2-SDS support, enhancing the electron transfer and boosting the formation of surface oxygen vacancies.

The chemical and coordination environments of Ce atoms were investigated by Ce L_3 XANES and EXAFS spectroscopy. As shown in Fig. S5a (Supporting information), CeO_2, CeO_2-SDS, and Pt/CeO_2-SDS catalysts present a double absorption line at energies of 5729 and 5736 eV, which is typical of the characteristic peaks of Ce^{4+} ions [28]. After quenching or supporting Pt NPs, the obtained XANES spectra almost overlap. It can be attributed that the weak variation of surface structure is masked by the stable conformation of bulk structure. Thereby, the above three catalysts exhibit identical coordination information in subsequent EXAFS spectra (Fig. S5b in Supporting information) and Wavelet-transformed k^3-weighted EXAFS spectra (Fig. S5c in Supporting information). Three peaks located at 1.87, 3.62, and 4.28 Å are attributed to the Ce-O_1, Ce-Ce, and Ce-O_2 scattering paths, respectively. And the wavelet transforms (WT) in Fig. S5c are in good agreement with the EXAFS results, where the WT maximum at 4–6 $Å^{-1}$ and 8–10 $Å^{-1}$ is assigned to the Ce-O and Ce-Ce paths, respectively.

Subsequently, the surface elemental distribution and corresponding electronic state were investigated by X-ray photoelectron spectroscopy (XPS). In Fig. 2a, U′ (901.9 eV) and V′ (884.2 eV) are designated for Ce^{3+} ions, and other peaks are assigned to Ce^{4+} ions [29]. The relative ratios (R^b) of Ce^{3+} to Ce^{4+} ions were calculated and summarized in Table S2 (Supporting information). Generally, the appearance of low-valent Ce^{3+} ions is accompanied by the generation of O_{Vs}, strongly affecting the catalytic performance of deep oxidation. After introducing surface defects, the fractions of Ce^{3+} ions rise from 16.8% to 20.8%, which implies an increase in surface O_{Vs}, corresponding to an enhancement of oxidation ability. Comparatively, the R^b value of CeO_2-SDS catalyst declines (26.3% → 22.2%) after supporting Pt NPs, which can be attributed to the generated O_{Vs} promoting the adsorption and activation of O_2 molecules, resulting in the transformation from Ce^{3+}-O_V-Pt^{2+}-O_V-Ce^{3+} to Ce^{4+}-O^--Pt^{2+}-O^--Ce^{4+}.

As can be seen in Fig. 2b and Table S2, the fractions of Pt^{2+} ions (76.0 and 72.7 eV) and Pt^0 (74.3 and 71.0 eV) on the Pt/CeO_2 catalyst are 59.1% and 40.9%, respectively. After introducing surface defects by quenching, positive Pt^{2+} ions (84.6%) are dominant on the Pt/CeO_2-SDS catalyst. Combined with previous results of Ce 3d XPS, it can be deduced that there is a transformation from Ce^{4+}-O^{2-}-Ce^{4+}-O^{2-}-Ce^{4+} to Ce^{3+}-O_V-Pt^{2+}-O_V-Ce^{3+} after introducing Pt

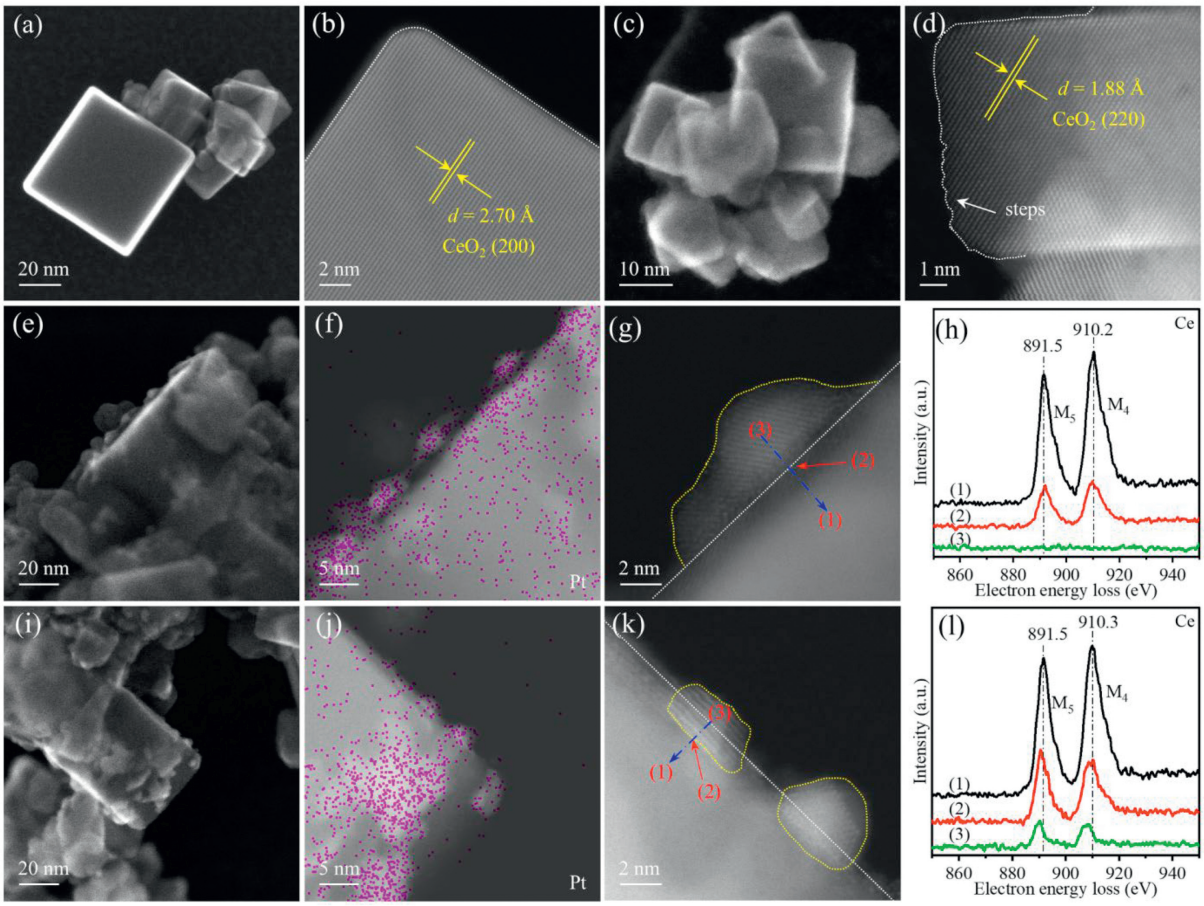

Fig. 1. Secondary electron scanning transmission electron microscopy (SE-STEM) images of (a) CeO_2, (c) CeO_2-SDS, (e) Pt/CeO_2 and (i) Pt/CeO_2-SDS catalysts. High resolution annular dark filed STEM (ADF-STEM) images of (b) CeO_2 and (d) CeO_2-SDS catalysts. EDS maps of Pt element over (f) Pt/CeO_2 and (j) Pt/CeO_2-SDS catalysts. ADF-STEM images of the Pt NPs on (g) Pt/CeO_2 and (k) Pt/CeO_2-SDS catalysts and corresponding (h, l) EELS spectra of Ce $M_{4,5}$-edge acquired across the Pt-CeO_2 interface.

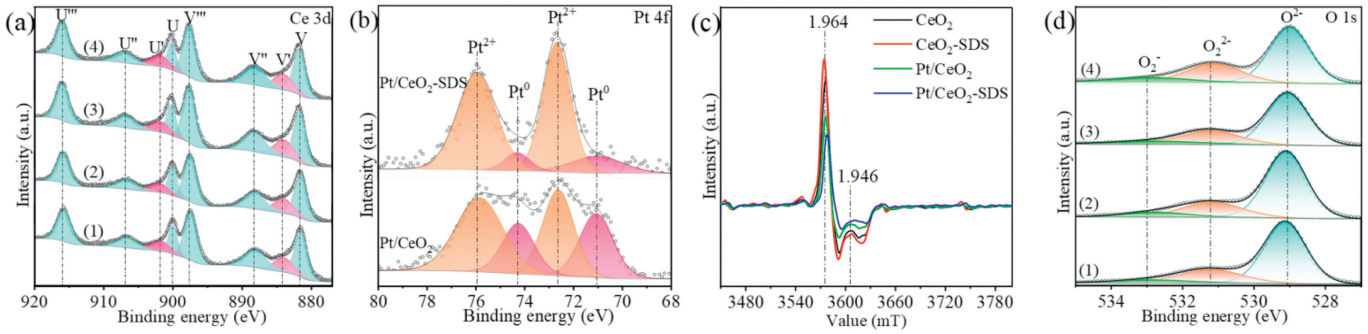

Fig. 2. Ce 3d (a), Pt 4f (b), O 1s (d) XPS and EPR (c) spectra of CeO_2 and Pt/CeO_2 catalysts: (1) CeO_2, (2) CeO_2-SDS, (3) Pt/CeO_2, (4) Pt/CeO_2-SDS.

NPs, well consistent with the above EELS results. Then, electron paramagnetic resonance (EPR) spectroscopy was further employed to investigate the distribution of O_{Vs} and Ce^{3+} ions. As shown in Fig. 2c, all catalysts exhibit two main peaks at g factors of 1.964 and 1.946, which further confirms the existence of paramagnetic Ce^{3+} species in fcc CeO_2 [30]. The density of Ce^{3+} and O_{Vs} can be increased by quenching, while it is decreased after supporting Pt NPs, indicating the transformation from Ce^{3+}-O_V-Pt^{2+}-O_V-Ce^{3+} to Ce^{4+}-O^--Pt^{2+}-O^--Ce^{4+}. According to previous literatures [30], the absence of O_{Vs} signal in all catalysts is attributed to the contribution of isolated O_{Vs} on the {100} facet to the Ce^{3+} paramagnetic signals. The charge derived from isolated O_{Vs} is localized on Ce ions in the second coordination shell, resulting in two paramagnetic Ce^{3+} ions [31].

In Fig. 2d, O 1s spectra were deconvoluted to adsorbed oxygen (O_A: O_2^-, 533.0 eV; O_2^{2-}, 531.2 eV) and lattice oxygen (O_L, 529.0 eV) [32]. The relative ratios (R^c) of O_A to O_L species were also calculated and collected in Table S2. After quenching, R^c values increase from 38.8% to 44.0%, corresponding to the increase of Ce^{3+} ions (16.8% → 20.8%). Thus, O_{Vs} are the main active sites on pure CeO_2. The introduction of Pt NPs significantly increases the R^c value from 38.8% to 52.3%. By comparing Pt/CeO_2 (52.3%) and Pt/CeO_2-SDS (59.3%) catalysts, it can be deduced that the geometric and electronic effects of the embedding structure significantly promote the formation of interfacial O_{Vs}, thereby facilitating the adsorption and the activation of O_2. Benefiting from the real-time replenishment of ROSs, the Pt/CeO_2-SDS catalyst performed the best oxidation capacity in all as-prepared samples.

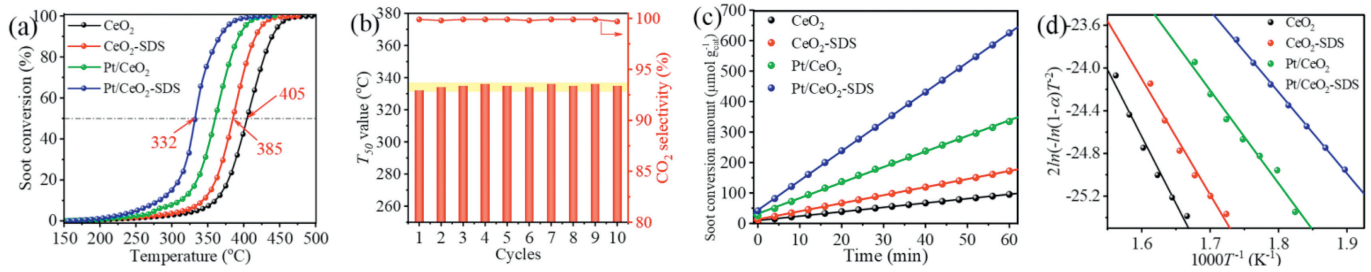

Fig. 3. Catalytic activity (a), cyclic stability (b), reaction rate (R_w) of soot particles at 280 °C (c) and Arrhenius plots of ln[-ln(1-α) T^{-2}] *vs.* T^{-1} at soot conversion of 5%–15% (d) of CeO_2, Pt/CeO_2 and Pt/CeO_2-SDS catalysts during soot oxidation.

In H_2-TPR profiles (Fig. S6 in Supporting information), two main reduction peaks are observed in both CeO_2 and CeO_2-SDS catalysts, which are attributed to the reduction of surface Ce^{4+} ions and bulk Ce^{4+} ions to Ce^{3+} ions, respectively [29]. The former peak shifts to low temperature (503 °C → 493 °C) after quenching, and the corresponding H_2 consumption increases from 87.6 μmol/g to 98.8 μmol/g (Table S3 in Supporting information). It indicates that the surface defects induced by quenching improve the reactivity of surface O_{latt}. After supporting Pt NPs, additional peaks are observed in 100–200 °C, belonging to the reduction of chemisorbed oxygen species on Pt NPs (Pt^{2+} ions) [33]. Compared with Pt/CeO_2 catalyst, Pt/CeO_2-SDS catalyst consumes more H_2 (75.4 μmol/g) at a lower temperature (132 °C), which indicates more Pt^{2+} ions on the CeO_2-SDS support, well consistent with the above results of Pt 4f XPS spectra. In addition, the temperatures of both reduction peaks belonging to CeO_2 shift to low temperatures and the H_2 consumption is higher than the corresponding support, attributing to the hydrogen spillover from Pt^0 to CeO_2. Among as-prepared catalysts, Pt/CeO_2-SDS catalyst consumes the most H_2 (116.2 μmol/g) at lowest temperature (371 °C), which further verifies the enhanced MSI by embedding structure. Similar to previous results of H_2-TPR, both surface defects and the resulted embedding structure can significantly improve the oxidation ability and capacity for NO (Fig. S7 in Supporting information). Among as-prepared catalysts, Pt/CeO_2-SDS catalyst produces the most gaseous NO_2 at relatively low temperatures, which will significantly promote the oxidation of soot particles. Thus, it can be concluded that: After quenching, abundant surface defects (O_{Vs}) formed on the surface of CeO_2 cubes, which improve the adsorption and activation of molecular O_2. In addition, it can also anchor Pt NPs, thus enhancing the interfacial electronic transmission between Pt NPs and CeO_2 {100} facet. Subsequently, it can significantly contribute to the replenishment of ROSs through interfacial the Ce^{3+}-O_V-Pt^{2+}-O_V-Ce^{3+} bond chains, thus facilitating the formation of gaseous NO_2.

The catalytic performance of CeO_2 and Pt/CeO_2 catalysts for soot oxidation was evaluated by soot-TPO tests. As displayed in Table S4 (Supporting information), the spontaneous oxidation of soot particles is extremely difficult, with T_{50} and $S_{CO_2}{}^m$ values of 572 °C and 67.9%, respectively. CeO_2 nanocubes present superior catalytic performance during soot oxidation, whose T_{50} value is 405 °C (Fig. 3a and Table S4). After quenching, the T_{50} value further declines by 20 °C, and the CO_2 selectivity is maintained at 100%. It can be ascribed that quenching induces the distortion of surface [CeO_6] units and the increase of surface O_{Vs}, boosting the adsorption and activation of molecular O_2 and NO. The T_{50} values of Pt/CeO_2 and Pt/CeO_2-SDS catalysts are 360 and 332 °C, respectively. The discrepancy is attributed that the enhanced interfacial electronic transmission by embedding structure boosts the formation of interfacial Ce^{4+}-O^--Pt^{2+}-O^--Ce^{4+} bond chains, significantly promoting the redox ability and capacity. In addition, the unique geometric structure also improves the subsequent cyclic stability of the Pt/CeO_2-SDS catalyst. As displayed in Fig. 3b, the T_{50} value of Pt/CeO_2-SDS catalyst always stabilizes at 335 °C. And the Pt loading (1.3 wt%) and embedding structure are well maintained after ten cycles, as confirmed by the ICP-OES and high-resolution STEM images (Fig. S8 in Supporting information). In addition, both the conversion rate of soot particles and CO_2 stability are stable during long-term soot-TPO experiments (Fig. S9 in Supporting information), which further confirm the superior stability of Pt/CeO_2-SDS catalyst. The superior catalytic activity and stability ensure that the Pt/CeO_2-SDS catalyst (Table S5 in Supporting information) can be a promising candidate for industrial applications.

Then, turnover frequency (TOF) and apparent activation energy (E_a) were further employed to investigate the intrinsic oxidation activity. TOF_O is defined as the quotient of the reaction rate (R_w) and the amount of ROSs (O* amount), which were obtained through the isothermal reaction at 280 °C. Additionally, TOF_{Pt} is also considered, which is defined as the ratio of reaction rate (R_w) to the Pt content. As can be seen in Fig. 3c and Table S4, the order of R_w values is well consistent with catalytic performance during soot-TPO tests. Surface defects increase the R_w value of the CeO_2 catalyst from 1.43 μmol g^{-1} min^{-1} to 2.64 μmol g^{-1} min^{-1}. And the resulting enhanced MSI increases the R_w value further to 9.69 μmol g^{-1} min^{-1}, supporting its lowest ignition activity (T_{10} = 280 °C) mentioned above. Additionally, the O* amount is another crucial index to quantify the intrinsic activity. As summarized in Fig. S10 and Table S4 (Supporting information), surface defects induced by quenching indeed improves the storage capacity of ROSs on the CeO_2, deriving from the dissociation of molecular O_2 on the surface O_{Vs}, well consistent with the above results. Among the four catalysts, the Pt/CeO_2-SDS catalyst possesses the highest O* amount (199.44 μmol/g), almost 1.5 times as much as the Pt/CeO_2 catalyst. It is further confirmed that the interfacial Ce^{3+}-O_V-Pt^{2+}-O_V-Ce^{3+} bond chains induced by embedding structure can significantly promote the adsorption and activation of molecular O_2, supporting the above H_2-TPR and CO-TPSR results. Both TOF_O and TOF_{Pt} values also present a similar trend to the above results, where the Pt/CeO_2-SDS catalyst performs the highest TOF_O (2.915 h^{-1}) and TOF_{Pt} (8.725 h^{-1}) values. Arrhenius plots and the resulting E_a values also support the results mentioned above (Fig. 3d and Table S4), it is extremely hard to oxidize soot particles with pure O_2 and NO, whose energy barrier is 185 kJ/mol [34]. After introducing as-prepared catalysts, the corresponding energy barrier decreases to 63.7 kJ/mol, corresponding to their best catalytic performance during soot oxidation. According to above TOF and E_a values, the enhanced interfacial electronic transmission by embedding structure presents the best adsorption-activation ability and capacity for O_2 and NO, thus promoting the oxidation of soot particles.

As a strong oxidizer with high mobility, NO_x plays a crucial role in boosting the high-efficient conversion of soot particles at low temperatures (Fig. S11 in Supporting information). Thus, the *in-situ* DRIFTS were further performed to elucidate the role of surface defects and embedding structure during NO oxidation. Firstly, the adsorption behavior of NO was investigated at 20 °C (Fig. S12 in

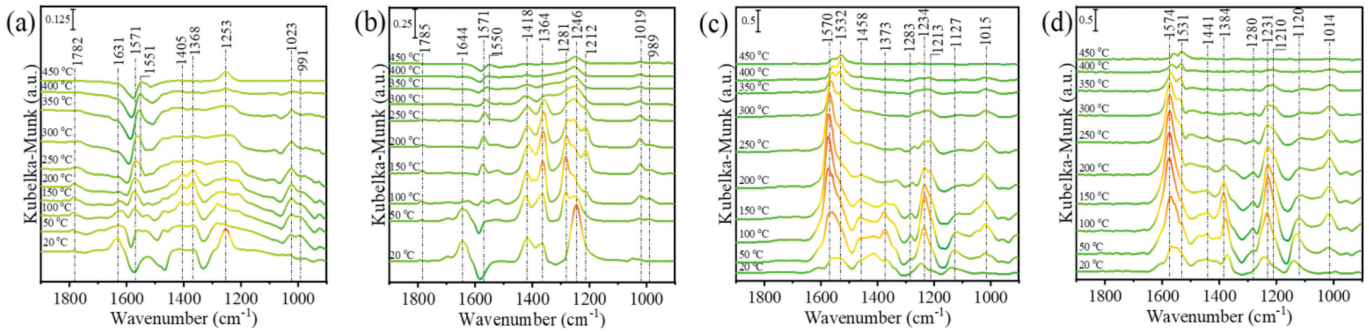

Fig. 4. *In-situ* DRIFTS of NO oxidation over CeO_2, Pt/CeO_2 and Pt/CeO_2-SDS catalysts: (a) CeO_2, (b) CeO_2-SDS, (c) Pt/CeO_2, (d) Pt/CeO_2-SDS.

Supporting information). For CeO_2 and CeO_2-SDS catalysts, the two sets of peaks at 1633–1627 and 1253–1246 cm^{-1} are respectively designated to bidentate and bridging nitrates (Table S6 in Supporting information) [35], which is relatively stable and unaffected by O_2 adsorption. In addition, the introducing of O_2 also produces two new peaks at 1422–1417 and 1368 cm^{-1}, which are attributed to nitro compound M-NO_2 (Table S6) [36,37]. In contrast, the main forms of adsorbed NO_x species on Pt/CeO_2 and Pt/CeO_2-SDS catalysts are monodentate nitrates (1557–1458 cm^{-1}) and the nitro compound M-NO_2 [32,35]. The intensity of adsorbed NO_x species is significantly weakened after supporting Pt NPs. Combined with the result of NO-TPO, the surface defects can promote the adsorption of NO_x on pure CeO_2, which gradually decomposes into NO_2 with rising temperature. After introducing Pt NPs, the adsorption and desorption of NO are no longer the rate-determining steps during NO oxidation. Then, *in-situ* DRIFTS of NO oxidation at elevated temperatures were performed to prove the above results. As can be seen from Figs. 4a and b, the signal of bridging nitrate and nitro compound is obviously enhanced by surface defects but gradually attenuated with the increasing temperature. It well supports the NO-TPO result that the gaseous NO_2 on pure CeO_2 catalysts originates from the decomposition of surface nitrites. As for Pt/CeO_2 and Pt/CeO_2-SDS catalysts (Figs. 4c and d), there is a little difference in surface nitrate species. In light of the results of H_2-TPR, XPS, and anaerobic titration, it is verified that the adsorption and activation of molecular O_2 is rate-determining step in the present system.

Finally, DFT calculations were performed to prove the regeneration path of ROSs. It can be seen from the diagram of differential charge density (Fig. S13 in Supporting information) that more pronounced interfacial charge accumulation is observed on the Pt/CeO_2-SDS catalyst compared with the Pt/CeO_2 catalyst. It can facilitate the activation of interfacial O_{latt} and the adsorption of O_2 [38,39]. Thus, the formation energy of interfacial O_{Vs} in Pt/CeO_2-SDS catalyst (−0.78 eV) is slightly lower than that of Pt/CeO_2 catalyst (−0.38 eV) (Fig. 5). Then, O_2 can be captured by the interfacial O_{Vs} of Pt/CeO_2-SDS catalyst and Pt/CeO_2 catalyst with an energy of −0.42 eV and −0.19 eV, respectively. The lower O_2 adsorption energy of oxygen ($E_{ads}(O_2)$) implies higher oxygen storage, well consistent with the above results of H_2-TPR and O* amount. The Bader charges (Fig. S14 in Supporting information) of adsorbed O_2 also support the results, which are respectively +0.94 |e| and +0.66 |e| for Pt/CeO_2-SDS catalyst and Pt/CeO_2 catalyst. Subsequently, the chemisorbed O_2 will dissociate into two active O* atoms, whose energy barrier (E_a') can reflect the refresh rate of ROSs. Here, E_a' values of Pt/CeO_2-SDS catalyst and Pt/CeO_2 catalyst are 0.33 eV and 0.68 eV, respectively. Combined with the optimized structures, it is obvious that the embedding structure facilitates the formation of [Ce-O_x-Pt_2] bond chains. In this way, PtO_x species are indirectly formed with the aid of interfacial [CeO_x] units, thus substantially promoting the adsorption and activation of O_2. The real-time replenishment of ROSs can be achieved, presenting superior redox performance during NO oxidation and soot oxidation.

In summary, we have developed a highly active and stable Pt/CeO_2-SDS catalyst for carbon oxidation. The Pt-NPs are anchored by surface defect sites of CeO_2 nanocubes, forming a unique embedding structure. AC-STEM images, EELS, and XPS spectra con-

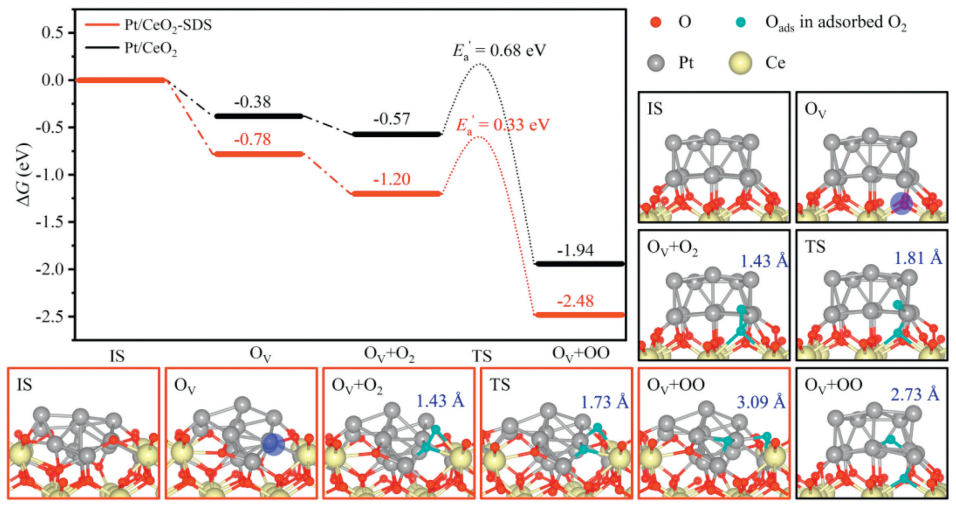

Fig. 5. The renewal paths for ROSs over Pt/CeO_2 and Pt/CeO_2-SDS catalysts.

firmed the formation of distinctive geometric structure, which enhance the MSI between Pt NPs and CeO_2-{100} support, facilitating more significant electron transfer with the formation of [Ce-O_x-Pt_2] bond chains. As a result, the high-active PtO_x species are indirectly formed with the aid of interfacial [CeO_x] units, which significantly activate the surface lattice oxygen and boost the dissociation of chemisorbed O_2. This leads to a notable increase in the amount of ROSs from 133.68 μmol/g to 199.44 μmol/g. The real-time replenishment of ROSs greatly promotes the formation of gaseous NO_2 and the conversion of soot particles. The combined geometric and electronic effects of the embedding structure ensure that Pt/CeO_2-SDS catalyst exhibited superior catalytic activity during soot oxidation (T_{50} = 332 °C, TOF = 2.915 h^{-1} and E_a = 63.7 kJ/mol). In addition, the superior catalytic performance was superior performance is well maintained after 5 cycles, positioning this catalyst as a promising candidate for future applications. This study sheds light on the crucial role of surface defects in enhancing interfacial electronic transmission, offering a promising strategy to enhance the activity and durability of supported noble metal catalysts.

Declaration of competing interest

The authors declare that they have no known competing financial interests or personal relationships that could have appeared to influence the work reported in this paper.

CRediT authorship contribution statement

Peng Zhang: Writing – original draft, Methodology, Investigation, Formal analysis, Conceptualization. **Yitao Yang:** Methodology, Investigation, Formal analysis, Conceptualization. **Tian Qin:** Investigation, Data curation. **Xueqiu Wu:** Methodology, Formal analysis, Data curation. **Yuechang Wei:** Writing – review & editing, Visualization, Validation, Supervision. **Jing Xiong:** Validation, Supervision, Data curation. **Xi Liu:** Supervision, Resources, Data curation. **Yu Wang:** Writing – review & editing, Visualization, Validation, Supervision, Data curation. **Zhen Zhao:** Visualization, Validation, Supervision. **Jinqing Jiao:** Writing – review & editing, Visualization, Validation, Supervision. **Liwei Chen:** Visualization, Validation, Supervision.

Acknowledgments

The authors wish to thank facility support of the 4B9A beamline of Beijing Synchrotron Radiation Facility (BSRF). This work was supported by the Beijing Nova Program (No. 20220484215), National Key Research and Development Program of China (Nos. 2022YFB3504100, 2022YFB3506200, 2021YFA1500300 and 2022YFA1500146) and National Natural Science Foundation of China (Nos. 22376217, 22208373, 22272090 and 22272106).

Supplementary materials

Supplementary material associated with this article can be found, in the online version, at doi:10.1016/j.cclet.2024.110396.

References

[1] R.H. Yan, X. Peng, W.W. Lin, et al., Environ. Sci. Technol. 56 (2022) 6996–7005.
[2] M. Wang, Y. Zhang, Y.B. Yu, W.P. Shan, H. He, Chin. Chem. Lett. 36 (2025) 109928.
[3] T.V. Johnson, SAE Int. J. Fuels Lubr. 2 (2009) 1–12.
[4] C.L. Zhang, D. Yu, C. Peng, et al., Appl. Catal. B 319 (2022) 121946.
[5] J. Xiong, Z.G. Li, P. Zhang, et al., Chin. Chem. Lett. 32 (2021) 1447–1450.
[6] P. Legutko, P. Stelmachowski, X.H. Yu, et al., ACS Catal. 13 (2023) 3395–3418.
[7] J. Shao, X.E. Lan, C.X. Zhang, C.M. Cao, Y.F. Yu, Chin. Chem. Lett. 33 (2022) 1763–1771.
[8] J.H. Lee, D.Y. Jo, J.W. Choung, et al., J. Hazard. Mater. 403 (2021) 124085.
[9] S.Y. Ma, F. Dong, S.X. Wu, et al., Appl. Catal. B 354 (2024) 124152.
[10] P. Zhang, J. Xiong, Y.C. Wei, et al., J. Catal. 398 (2021) 109–122.
[11] W.L. Fu, Z.H. Li, Y.P. Wang, Y.M. Sun, Y.Q. Dai, Chem. Eng. J. 401 (2020) 126013.
[12] M.A. Salaev, A.A. Salaeva, T.S. Kharlamova, G.V. Mamontov, Appl. Catal. B 295 (2021) 120286.
[13] L.J. Zhang, R.H. Chen, Y. Tu, et al., ACS Catal. 13 (2023) 2202–2213.
[14] Y. Chen, Q. Wan, L.R. Cao, et al., J. Catal. 415 (2022) 174–185.
[15] C. Zou, G.X. Li, K. Zhang, et al., Mater. Today Nano 24 (2023) 100411.
[16] N.H. Fu, X. Liang, X.L. Wang, et al., J. Am. Chem. Soc. 145 (2023) 9540–9547.
[17] Y.P. Wang, Z.H. Li, W.L. Fu, Y.M. Sun, Y.Q. Dai, Adv. Fiber Mater. 4 (2022) 1278–1289.
[18] J.H. Lee, D.J. Shin, E.W. Lee, et al., Appl. Catal. B 305 (2022) 121038.
[19] T.W. van Deelen, C. Hernández Mejía, K.P. de Jong, Nat. Catal. 2 (2019) 955–970.
[20] S.H. Xie, W. Tan, C.Y. Wang, et al., J. Catal. 405 (2022) 236–248.
[21] K.L. Ding, A. Gulec, A.M. Johnson, et al., Science 350 (2015) 189–192.
[22] J.S. Du, T. Bian, J.J. Yu, et al., Adv. Sci. 4 (2017) 1700056.
[23] J. Yu, X.T. Qin, Y.S. Yang, et al., J. Am. Chem. Soc. 146 (2024) 1071–1080.
[24] C. Schilling, A. Hofmann, C. Hess, M.V. Ganduglia-Pirovano, J. Phys. Chem. C 121 (2017) 20834–20849.
[25] F. Wang, C.M. Li, X.Y. Zhang, et al., J. Catal. 329 (2015) 177–186.
[26] M.Z. Wang, Y.G. Zhang, Z. Wu, et al., Chem. Eng. J. 450 (2022) 138171.
[27] H.F. Xu, Y.F. Wang, J. Nucl. Mater. 265 (1999) 117–123.
[28] F. Wang, S. He, H. Chen, et al., J. Am. Chem. Soc. 138 (2016) 6298–6305.
[29] Y.C. Wei, Y.L. Zhang, P. Zhang, et al., Environ. Sci. Technol. 54 (2020) 2002–2011.
[30] Y. Cao, L. Zhao, T. Gutmann, et al., J. Phys. Chem. C 122 (2018) 20402–20409.
[31] E. Shoko, M.F. Smith, R.H. McKenzie, J. Phys. Condens. Matter 22 (2010) 223201.
[32] P. Zhang, M. Yang, D.W. Han, et al., Appl. Catal. B 321 (2023) 122077.
[33] S.H. Xie, L.P. Liu, Y. Lu, et al., J. Am. Chem. Soc. 144 (2022) 21255–21266.
[34] B. Cui, L.J. Zhou, K. Li, et al., Appl. Catal. B 267 (2020) 118670.
[35] G. Busca, V. Lorenzelli, J. Catal. 72 (1981) 303–313.
[36] K.I. Hadjiivanov, Catal. Rev. 42 (2000) 71–144.
[37] W.B. Chen, X.D. Wang, S.Z. Xu, Chem. Eng. J. 460 (2023) 141801.
[38] C.Z. He, R.S. Sun, L. Fu, et al., Chin. Chem. Lett. 33 (2022) 527–532.
[39] F. Yuan, R.S. Sun, L. Fu, G.Z. Zhao, Chin. Chem. Lett. 33 (2022) 2188–2194.